Manipulation and statistical analysis of the fluid flow of polymer semiconductor solutions during meniscus-guided coating

Leo Shaw, Ying Diao, Geoffrey C. Martin-Noble, Hongping Yan, Pascal Hayoz, R. Thomas Weitz, Daniel Kaelblein*, Michael F. Toney,* and Zhenan Bao*

Recent work in structure–processing relationships of polymer semiconductors have demonstrated the versatility and control of thin-film microstructure offered by meniscus-guided coating (MGC) techniques. Here, we analyze the qualitative and quantitative aspects of solution shearing, a model MGC method, using coating blades augmented with arrays of pillars. The pillars induce local regions of high strain rates—both shear and extensional—not otherwise possible with unmodified blades, and we use fluid mechanical simulations to model and study a variety of pillar spacings and densities. We then perform a statistical analysis of 130 simulation variables to find correlations with three dependent variables of interest: thin-film degree of crystallinity and transistor field-effect mobilities for charge-transport parallel (μ_{para}) and perpendicular (μ_{perp}) to the coating direction. Our study suggests that simple fluid mechanical models can reproduce substantive correlations between the induced fluid flow and important performance metrics, providing a methodology for optimizing blade design.

Polymer semiconductors have opened up a new frontier of electronics that can be flexible, stretchable, implantable, or biodegradable. While the chemical and electronic properties of these materials are important for their function as the active material in organic electronic devices, the manner by which these organic semiconductors are deposited onto a substrate can significantly influence its charge-transport properties.

While a variety of techniques have been investigated to enhance charge-transport behavior, there are few reports approaching the issue in terms of the fluid dynamical considerations relevant during deposition from the solution phase. In this article, we analyze the fluid flow that occurs during thin-film deposition by solution shearing, a representative meniscus-guided coating method amenable to high-throughput processing. We investigate a variety of variables related to fluid flow that can be estimated from fluid mechanical simulations of solution shearing with a coating blade patterned with a regular array of pillars used to induce higher fluid strain rates. We find correlations suggestive of underlying relationships between strain rates associated with certain directions and polymer charge-transport properties in the final deposited film. This article establishes a statistical approach using simulation data that can guide patterned blade design to enhance polymer deposition and realize high-performance devices.

Introduction

The promise of organic electronics in recent years has been to fill applications spaces that are difficult to reach with silicon-based devices. Flexible, stretchable, implantable, biodegradable, self-healing, and translucent electronics have been demonstrated by taking advantage of the tunable properties of organic semiconductors (OSCs), specifically, soluble polymeric ones.[1–3] The commercial realization of these devices depends in part on economic considerations and is particularly aided by the development of high-throughput, large-area processes such as meniscus-guided coating (MGC) methods, a class of unidirectional deposition techniques amenable to scale-up as industrially relevant solution-phase roll-to-roll (R2R) coating processes.[4,5] Deposition parameters such as coating speed, temperature, and solvent choice can have a dramatic influence on the resulting thin-film microstructure of the OSC active layer and must be carefully controlled, often making scale-up from laboratory proofs-of-concept nontrivial.[4] Because of this difficulty, a fundamental understanding of the processes related to solid-film formation—fluid mechanical flows, solvent evaporation, polymer nucleation, and crystallization, among others—is a crucial foundation upon which more complex methods can be developed and used to enhance desirable properties such as charge-transport or alignment.[5]

Leo Shaw, Department of Chemical Engineering, Stanford University, USA
Ying Diao, Department of Chemical and Biomolecular Engineering, University of Illinois at Urbana-Champaign, USA
Geoffrey C. Martin-Noble, Department of Chemical Engineering, Stanford University, USA
Hongping Yan, Stanford Synchrotron Radiation Lightsource, SLAC National Accelerator Laboratory, Menlo Park, USA
Pascal Hayoz, BASF Schweiz AG, Schweizerhalle, Switzerland
R. Thomas Weitz, I. Physikalisches Institut, Georg-August-Universität Göttingen, Germany
Daniel Kaelblein, BASF SE, Ludwigshafen, Germany
Michael F. Toney, Department of Chemical and Biological Engineering, University of Colorado Boulder, USA
Zhenan Bao, Department of Chemical Engineering, Stanford University, USA
*Corresponding authors: Daniel Kaelblein, daniel.kaelblein@basf.com; Michael F. Toney, michael.toney@colorado.edu; Zhenan Bao, zbao@stanford.edu
doi:10.1557/mrs.2020.306

Recent work probing these basic deposition processes has substantially advanced our understanding of solution-phase thin-film polymer OSC deposition and often highlights important tools needed to guide future research. For example, x-ray scattering has been an important part in the study of single and multicomponent semicrystalline polymer thin films, with the more common *ex situ* measurements useful for determining π-stacking and lamella stacking distances in the ordered film fraction and *in situ* experiments necessary for observing the temporally resolved evolution of crystallites during deposition.[6] In addition to these methods, the rise of cost-effective high-performance computing has opened up numerical simulation as another technique that can be utilized for the study of polymer OSC film solidification. Molecular dynamics, Monte Carlo simulations, and other methods are often used in the field to model deposition at size scales ranging from atoms ($\approx 10^0$–10^2 Å) to crystalline domains ($\approx 10^2$–10^3 Å).[7–10] The experimental demonstration of enhanced deposition techniques that directly influence fluid flow during coating has suggested the use of fluid mechanical simulation as another important tool for predicting the resulting thin-film microstructure and, ultimately, charge-transport performance.[11]

Previous work on solution shearing, a prototypical MGC method similar to blade coating, inspires the engineering of techniques to induce phenomena beneficial to performance of the coated solid film. The FLUENCE method developed by Diao et al. couples selectively wetting substrate patterning with a coating blade possessing an array of crescent-shaped pillars.[12] These protrusions alter the velocity field within the solution reservoir and allow for the deposition of millimeter-wide, centimeter-long single-crystalline thin films of a model small-molecule OSC 6,13-bis(triisopropylsilylethynyl)pentacene (TIPS-pentacene). The excellent control of nucleation and crystal growth facilitates superior film morphologies and large single-crystalline domains, allowing fabricated devices using the thin film of active material to achieve high charge carrier mobilities.

In the case of polymer OSCs, the control of polymer nucleation is especially useful for photovoltaic applications because small domain sizes on the order of the exciton diffusion length are needed in bulk heterojunction solar cells to reduce charge recombination and increase overall power conversion efficiency.[13] Moreover, the deposition of single-component polymer solutions can also benefit from control of nucleation, especially if an increase in the crystalline fraction of the film enhances charge transport. In either case, (semi-crystalline) polymer nucleation is enhanced by increased strain rates in the solution, which can cause free polymer molecules to overcome entropic barriers and adopt molecular conformations favorable for better intermolecular packing. MGC techniques involving the use of solid coating heads are particularly suited to impart high strain rates to the coating solution because the liquid–solid interface between the ink and head induces higher strain rates than for a free interface (e.g., dip coating). Further enhancement of MGC processes

in this regard is possible by engineering effective designs to pattern the coating head with features that can induce fluid flows not possible otherwise.[11–14]

In this article, we use the original design of the patterned coating blades used in FLUENCE to determine the effect of different pillar array dimensions and densities. In particular, we perform fluid mechanical simulations and calculate quantitative metrics from the numerical solution to correlate with the thin-film morphology and charge-transport performance of deposited polymer films of PDPP3T, a donor–acceptor alternating copolymer (discussed further below) sensitive to strain-rate differences during deposition. Our goal is to use a simplified computational model to uncover general principles useful for the future design of modified coating blades and for the elucidation of important parameters that can be tuned and engineered in future work.

Fluid mechanical simulation

The resulting film crystallinity and morphology after deposition is highly dependent on the chemical nature of the polymer OSC, making predictions challenging. Nonetheless, a simulation of the expected strain rate for a given deposition geometry and set of deposition conditions can be useful for comparing the effectiveness of the particular design of a coating blade patterned with pillars. If the strain rates achievable with MGC without any patterning of the coating head or blade can induce differences in crystallinity, increasing the attainable strain rates with solid pillars may enhance polymer nucleation further. In principle, because strain-induced nucleation can yield stable crystallite nuclei in solution and can occur anywhere in the solution upstream of the contact line, knowledge of the fluid flow can be a powerful tool in guiding blade design and in predicting final film morphology. For this reason, we perform simulations of a variety of arrays of crescent-shaped pillars to evaluate their usefulness in predicting the morphology of deposited polymer films. We defer to an analysis of pillar shape and its impact on fluid flow to future work.

While strain rate is implicated in the alignment and nucleation processes, discussion about its influence on specific systems is often qualitative, and to our knowledge, there are virtually no reports in the literature for semiconducting polymer depositions that use direct quantitative metrics to compare the imposed strain as a function of deposition-related variables. Without a quantitative measure of the induced strain rates on the solution during deposition, it is difficult to accurately gauge the effects of changing certain parameters. In our case, we wish to simulate and observe the effect of pillar density and array spacing on solution flow beneath the coating blade, so for this purpose, we determine for each mesh element in the simulation box the rate-of-strain tensor **E**, a symmetric second-rank tensor calculated from the velocity gradient (i.e., the Jacobian of the velocity as a vector-valued function) that precisely describes the strain rate.[15] **E** contains six unique tensor elements, and when written as a two-dimensional (2D) matrix, the three diagonal elements describe the

extensional strain rate, and the three unique off-diagonal elements describe the shear strain rate.

In addition to these six terms, we also calculate the overall effective strain rate $\dot{\gamma}$ using the second invariant of $\mathbf{E}$,[16] which reduces the tensor to a scalar value more tractable for comparison across data sets. Because a polymer solution is an incompressible liquid, $\mathbf{E}$ is directly calculable from the first spatial derivatives of the velocity vector and is thus easily accessible from flow simulations. Moreover, we calculate the Frobenius norm of the rate-of-strain tensor $\|\mathbf{E}\|_F$ to represent the absolute magnitude of the total strain rate at any (mesh) element in the simulation box. The Frobenius norm is simply an extension of the standard Euclidean norm (the two norm) of a vector to a matrix. While rank-two tensors are sometimes written as 2D matrices, tensors themselves can be thought of as a generalized vector in an N-dimensional space: a tensor of rank (or order) 1 is a single array of N elements, and a rank-2 tensor is a 2D array with a total of $N \times N$ elements. We thus apply the Frobenius matrix norm by imagining the rank-two rate-of-strain tensor $\mathbf{E}$ as a square 3×3 matrix.

A mathematical discussion, summary of simulation results, and details on simulation parameters are provided in the Supporting Information section. Importantly, we use a simulation box pervading the volume close to the edge of the coating blade and impose simplifying assumptions on the boundary conditions. We also chose deposition parameters to mimic the real experimental conditions for the deposited films discussed here. We believe these choices do not limit the generality of our simulation results based on several empirical observations recorded during actual polymer thin-film deposition using solution shearing. We note that blade tilt angle has a minor effect on deposition for angles greater than 0° and less than about 20°. For large gap heights (>15 µm), the effect of the patterned pillars is significantly reduced, and the resulting films behave similarly to those deposited with unpatterned blades. Solvent evaporation rate largely influences the range of coating speeds accessible in the Landau–Levich regime, where the coating process itself has a direct influence on solid-film formation.[6] Finally, solution concentrations greater than ~1 wt% leads to improper dissolution and interference caused by gelation. Below this threshold, solutions of the polymer studied (discussed next) in 1,2,3,4-tetrahydronaphthalene (tetralin) revealed viscosities that were effectively identical to that of the neat solvent. Given these relatively low concentrations, we believe approximating the solution as a Newtonian fluid is warranted.

Each of these constraints allow us to reduce the simulation parameter space to a set of conditions we believe are most useful to reflect actual experimental conditions, and the restriction of the simulation box to the locus of highest influence by the pillars facilitates the feasibility of the calculations. Our goal is to determine whether such a mathematical treatment with these simplifications can nonetheless yield results that are correlated with experimentally observed properties so that future research can improve upon this work.
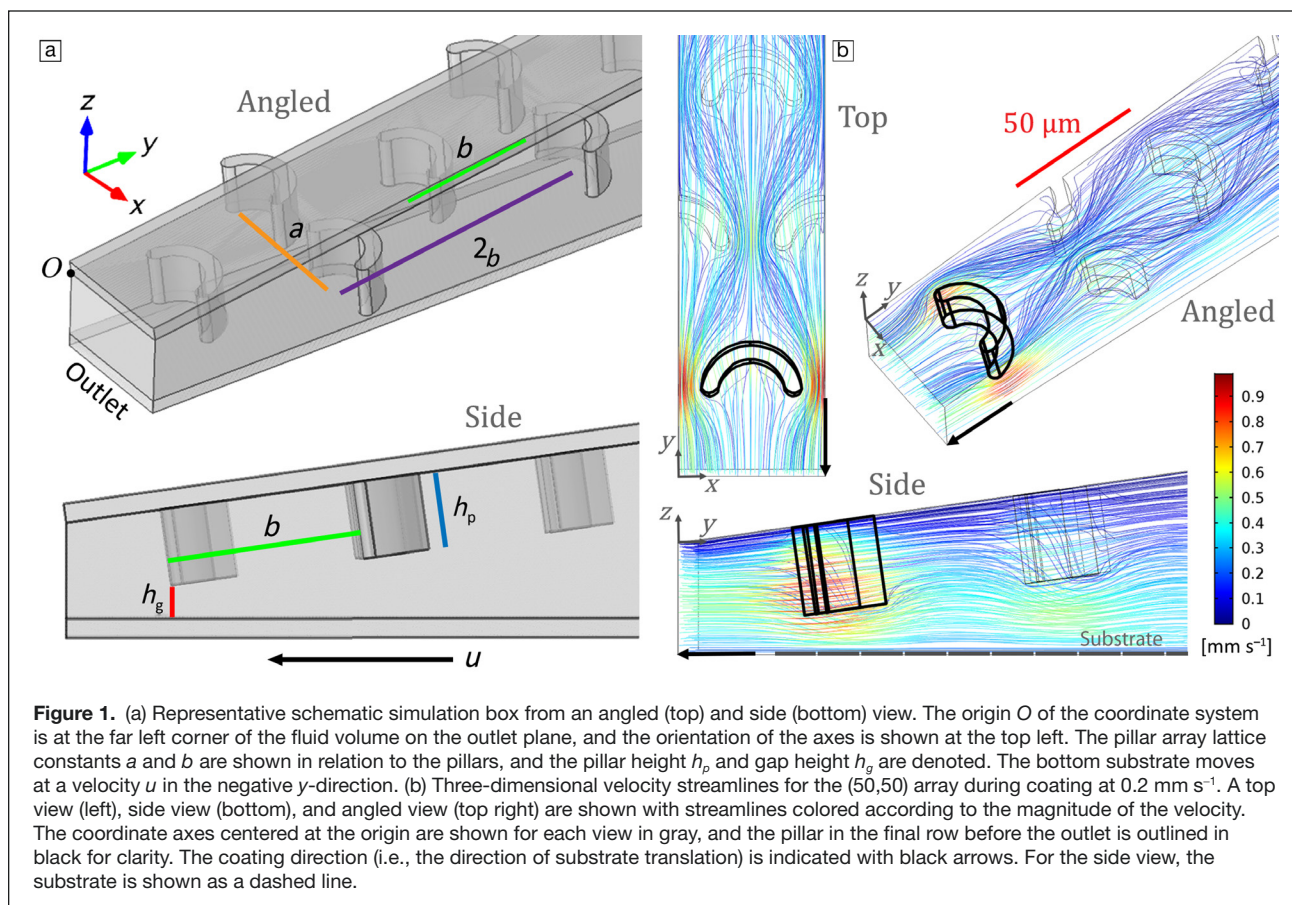
Results
Velocity and strain rate distributions

For our simulations, we model the patterned coating blades using a simulation box comprising five staggered rows of crescent-shaped pillars (height $h_p = 20$ µm, crescent inner radius: 11.5 µm, outer radius: 17.5 µm) that are convex against fluid flow moving primarily in the negative y-direction (**Figure 1**a). The first row is offset from the very edge of the coating blade close to the outlet by $a/2$, and an additional gap height h_g of 1 µm extends between the bottom of the pillar and the substrate surface. The coating blade is inclined at 8°, and the coating speed (substrate velocity) is chosen to be 0.2 mm s^{-1}. These parameters are chosen to be consistent with the experimental conditions used. We name the pillar arrays using an ordered (a, b) pair, where a is the distance (µm) in the x-direction between the centers of the circles that defines the crescent pillar, and b is the y-direction distance (µm) between the pillar rows (i.e., a is the interpillar distance and b is the interrow spacing).

Five rows of pillars are chosen because of the limitations in the maximum number of computational degrees of freedom allowed with the boundary conditions specified before the simulation becomes ill-conditioned or computationally infeasible; more pillars would increase the complexity of the mesh, requiring more boundary or initial conditions to fully specify the problem and find a solution. Furthermore, much of the pillars' influence on the flow field occurs because of the presence of the first two rows because they are close to the substrate surface and the solution outlet. We found that the addition of more rows of pillars to the smaller and simpler simulation models did not significantly affect the flow field close to the outlet, making additional rows of pillars ostensibly unnecessary.

In Figure 1b, three-dimensional (3D) velocity streamlines for the (50,50) array are shown as a representative simulation example. The relative influence of the first pillar row is clear: the highest velocities occur right before the outlet and specifically between the pillars within a row. Because the inclined coating blade causes this row to be closest to the bottom substrate, higher fluid pressures induce force on the fluid between the pillars within the final row as it exits through the outlet. The blade tilt also causes the rear, upstream pillars to be relatively far from the substrate so that most of the fluid flow bypasses the rear pillars by moving underneath them, as seen in the side view shown in Figure 1. Fluid flow within the array between the upstream pillars is thus relatively stagnant, meaning more fluid moves underneath the array until it encounters the final forward-most row (closest to the outlet). There is some acceleration in the positive z-direction, and fluid moving between the pillars experiences strong extensional and shear flow. These two pathways create a local region of relatively high strain rates, suggesting that any flow-induced phenomenon involving the polymer solute likely occurs there.

Given this general trend, we compare the effect of different pillar spacings and densities. **Figure 2** (top) shows the velocity fields for simulations corresponding to a vertical cut-plane
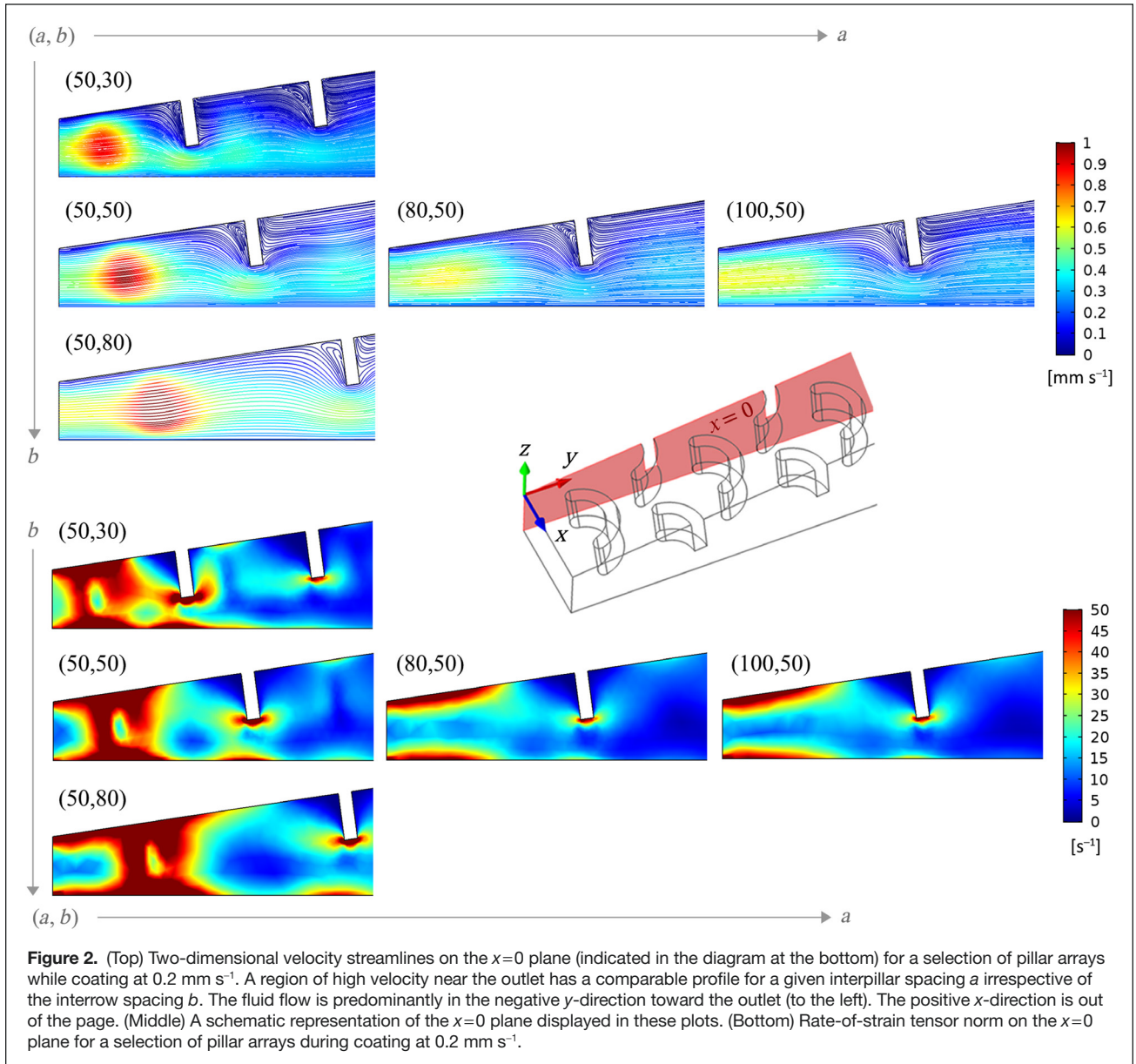
Figure 1. (a) Representative schematic simulation box from an angled (top) and side (bottom) view. The origin O of the coordinate system is at the far left corner of the fluid volume on the outlet plane, and the orientation of the axes is shown at the top left. The pillar array lattice constants a and b are shown in relation to the pillars, and the pillar height h_p and gap height h_g are denoted. The bottom substrate moves at a velocity u in the negative y-direction. (b) Three-dimensional velocity streamlines for the (50,50) array during coating at 0.2 mm s^{-1}. A top view (left), side view (bottom), and angled view (top right) are shown with streamlines colored according to the magnitude of the velocity. The coordinate axes centered at the origin are shown for each view in gray, and the pillar in the final row before the outlet is outlined in black for clarity. The coating direction (i.e., the direction of substrate translation) is indicated with black arrows. For the side view, the substrate is shown as a dashed line.

at $x=0$ for the (50,30), (50,50), (50,80), (80,50), and (100,50) arrays all with the same color scale for velocity. Only the magnitude of the y and z components of the velocity vector $\bar{v}$ are shown in these 2D velocity streamline representations. We can see that for an interpillar spacing a of 50 μm, a region of maximum velocity occurs relatively close to the simulation outlet. Although not shown in the images, the first row of pillars (which do not intersect the $x=0$ plane) directly induce the high velocity in this region as fluid is forced between two adjacent pillars. Comparing the arrays, we see that this region has a comparable velocity profile for a given interpillar spacing, a, irrespective of the interrow spacing, b. However, when we fix b and compare differing a, the velocity in this region dramatically decreases with increasing interpillar a. This indicates that the primary factor in increasing the fluid velocity is the spacing of the pillars within a row. Intuitively, the immediate cause of the increase in velocity is the size of the gap that the fluid is forced through and not some other property that is nonlocal to this specific region (the interrow spacing). We note that the region of high velocity shifts away from the outlet with increasing b, likely because of the direct effect of the first pillar row, which is slightly farther back from the outlet (based on our simulation specification).

From the velocity fields, we calculate the Frobenius norm of the rate-of-strain tensor $\|\mathbf{E}\|_F$ and depict their values on the

same vertical slices in Figure 2 (bottom). Here, we can directly visualize and compare the variations in tensor element magnitude caused by the different arrays. The shift of the high-velocity region away from the outlet with increasing b (as previously mentioned) is also reflected in the tensor norm representation. Interestingly, $\|\mathbf{E}\|_F$ appears high in a larger area for the highest b—(50,80)—while increasing a dramatically reduces $\|\mathbf{E}\|_F$ in the mid-gap region between the substrate and the blade near the outlet. While this may appear true locally, the volume-averaged Frobenius tensor norm $\|\mathbf{E}\|_F$ across all arrays is highest for the lowest interpillar and interrow spacing (**Figure 3**a). This result is intuitive since the averaging occurs over a larger volume for high a and b, but may have significance when considering the overall (average) influence of the pillars on the dissolved polymer molecules within the fluid volume. When we also look at the maximum $\|\mathbf{E}\|_{max}$ that occurs at any point in the simulation box (Figure 3b), we see the smallest a consistently achieves the highest $\|\mathbf{E}\|_{max}$ irrespective of b. In fact, an increase of 10 μm in a when $b=50$ μm causes appoximately a 40% drop in $\|\mathbf{E}\|_{max}$, indicating the crucial importance of small interpillar spacings for attaining high total strain rates in this geometry.

These results have some significance when considering the type of polymer molecule deposited. For strongly disordered yet semicrystalline polymers with a high density of torsional defects along their backbones, strong strain rates at some
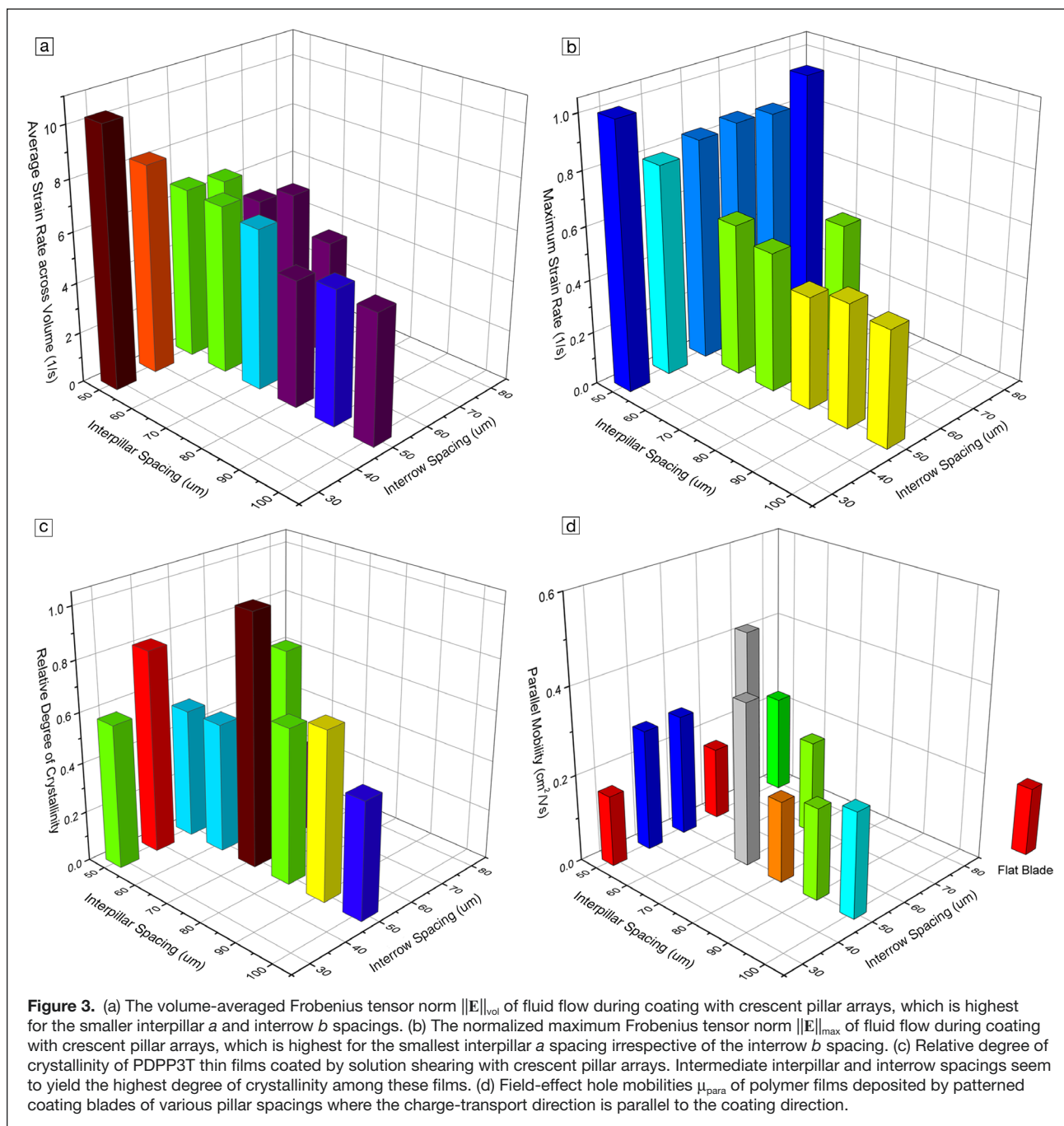
Figure 2. (Top) Two-dimensional velocity streamlines on the $x=0$ plane (indicated in the diagram at the bottom) for a selection of pillar arrays while coating at 0.2 mm s^{-1}. A region of high velocity near the outlet has a comparable profile for a given interpillar spacing a irrespective of the interrow spacing b. The fluid flow is predominantly in the negative y-direction toward the outlet (to the left). The positive x-direction is out of the page. (Middle) A schematic representation of the $x=0$ plane displayed in these plots. (Bottom) Rate-of-strain tensor norm on the $x=0$ plane for a selection of pillar arrays during coating at 0.2 mm s^{-1}.

point during fluid flow may be necessary for better molecular elongation[17] and an increased chance for more effective intermolecular interaction. On the other hand, if the threshold for polymer extension is not the limiting factor, larger overall strain rates throughout the solution volume may enhance intermolecular association, because extended polymer chains have more surface area for intra- and intermolecular interactions.

We note here that all strain rate tensor elements e_{ij} are weighted equally when calculating the Frobenius norm even though specific directional strain elements may be more important than others. We emphasize that while $\|\mathbf{E}\|_F$ is a convenient measure for quantitatively comparing our simulation data, only $|\dot{\gamma}|$ as calculated using the second invariant of $\mathbf{E}$ is related to the stress tensor $\mathbf{T}$ as found in the Cauchy momentum equation and used in the derivation of the general

Navier–Stokes equation. For incompressible Newtonian fluids, $\mathbf{T}$ varies as $2\,\mu\mathbf{E}$, where the proportionality constant μ is the (dynamic) shear viscosity. In the case of non-Newtonian behaviors, such as shear thinning or extensional thickening, μ can be expanded as a function of $\mathbf{E}$, similar to Carreau liquids.[18] Because our solutions are relatively dilute and consist of polymer with modest molecular weights, we assume classical Newtonian behavior.

To further characterize the types of strain occurring in each of the different regions of the pillar array, we perform particle tracing to determine exactly where the regions of strong strain rates are, which can be either positive or negative. We trace the flow originating from two points chosen so that their streamlines enter the pillar array (**Figure 4**). Starting with e_x (in red), we can see that the profiles are effectively identical in sign near
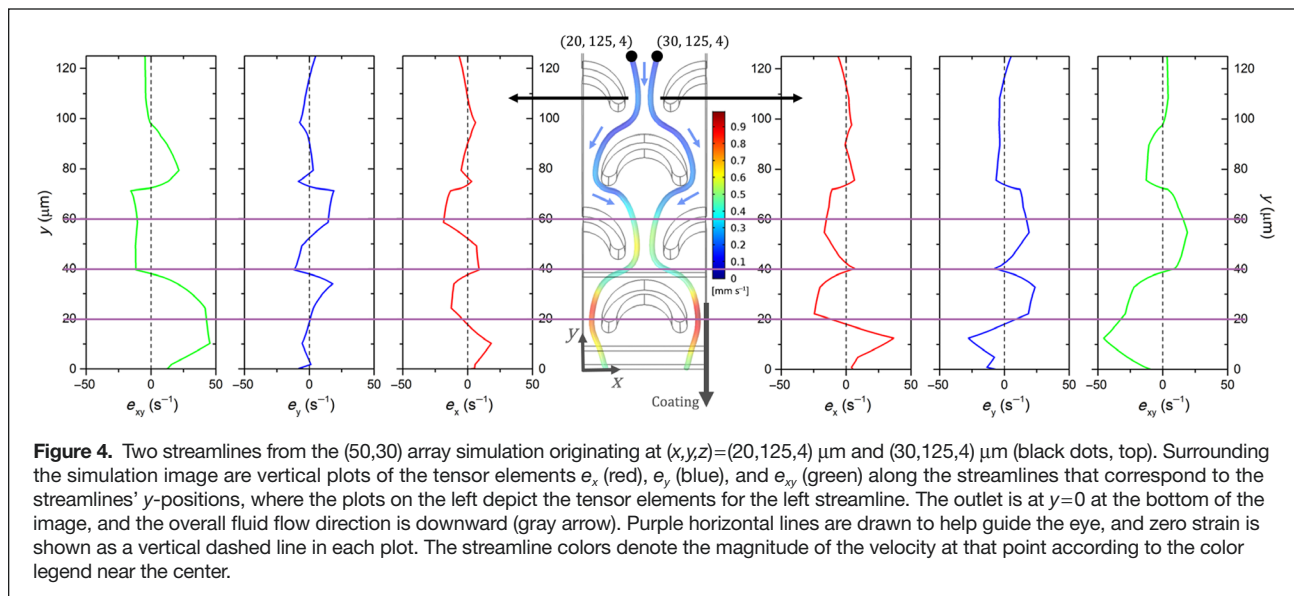
Figure 3. (a) The volume-averaged Frobenius tensor norm $\|\mathbf{E}\|_{vol}$ of fluid flow during coating with crescent pillar arrays, which is highest for the smaller interpillar *a* and interrow *b* spacings. (b) The normalized maximum Frobenius tensor norm $\|\mathbf{E}\|_{max}$ of fluid flow during coating with crescent pillar arrays, which is highest for the smallest interpillar *a* spacing irrespective of the interrow *b* spacing. (c) Relative degree of crystallinity of PDPP3T thin films coated by solution shearing with crescent pillar arrays. Intermediate interpillar and interrow spacings seem to yield the highest degree of crystallinity among these films. (d) Field-effect hole mobilities μ_{para} of polymer films deposited by patterned coating blades of various pillar spacings where the charge-transport direction is parallel to the coating direction.

the bottom pillar row—negative extensional strain occurs as fluid is about to enter the interpillar region ($20 < y < 40\,\mu$m), and positive strain occurs as the fluid exits ($0 < y < 20\,\mu$m). For the second pillar row up, e_x changes sign within the interpillar region as the acceleration (change in speed) between the pillars and the acceleration (change in direction) around the bottom pillar combine to produce a mixed effect. The pillar rows beyond the bottom two induce much smaller strain rates.

These results are similar for e_y (blue), except that the strain rates are positive and then negative as fluid passes through the final pillar row. These results are also consistent for flow

originating substantially below the pillar array (**Figure S1**). Despite the ostensible symmetry between these two streamlines, both extensional strain rates generally possess the same parity (sign) in the same regions. This is not true for the shear term e_{xy} (green), which exhibits relatively high shear strain rates of opposite sign for both regions ($0 < y < 40\,\mu$m). It is clear that the highest strain rates occur around the final pillar row.

Correlation with deposited thin films

With these simulation results, we turn our attention to films deposited using patterned coating blades directly

Figure 4. Two streamlines from the (50,30) array simulation originating at $(x,y,z)=(20,125,4)$ μm and $(30,125,4)$ μm (black dots, top). Surrounding the simulation image are vertical plots of the tensor elements e_x (red), e_y (blue), and e_{xy} (green) along the streamlines that correspond to the streamlines' y-positions, where the plots on the left depict the tensor elements for the left streamline. The outlet is at $y=0$ at the bottom of the image, and the overall fluid flow direction is downward (gray arrow). Purple horizontal lines are drawn to help guide the eye, and zero strain is shown as a vertical dashed line in each plot. The streamline colors denote the magnitude of the velocity at that point according to the color legend near the center.

corresponding to the dimensions used in the simulation. In this way, we can observe statistical correlations between real films and the calculated velocity and strain rate profiles. The ordered crystalline domains in semicrystalline conjugated polymer thin films typically play an important role in charge transport. Polymers with high crystallinity are often desirable for use in high-performance organic field-effect transistor devices, although a recent result has indicated that high crystallinity is not always a prerequisite for effective charge transport.[19–21] Precise control of the polymer nucleation and crystallite growth processes for semicrystalline polymer films deposited by MGC is difficult compared to small-molecule systems, which can be quite crystalline.[22] While theoretical and experimental work on homogeneous and heterogeneous nucleation in nonconjugated polymer systems is extensive, less effort has been focused on semiconducting polymers. The use of shear forces during a solution-phase processing technique is a general method to induce nucleation supported by a mature body of literature for conventional polymers.[23,24] There are only a few examples of the application of such techniques on polymer OSCs in devices for the specific purpose of realizing strain-induced polymer nucleation during deposition.[25,26] For example, coating blades patterned with short (≈ 5 μm) hexagonal pillars can manipulate the fluid dynamics of solution shearing during the deposition of all-polymer solar cells and enhance their performance.[13] By increasing extensional flow and the overall strain imparted on the solution—a blend of a semicrystalline donor polymer and amorphous acceptor polymer—strain-induced nucleation of the donor is enhanced, as demonstrated by the increase in the relative degree of crystallinity (rDoC) that increases solar cell performance. In particular, the overall power-conversion efficiency improved by nearly twofold. It is clear that because crystallization kinetics may play a significant role in overall device performance for certain applications, a knowledge of what factors facilitate

the ability to tune thin-film crystallinity is important for the continued design and control of polymer thin-film solution deposition.

We choose to study PDPP3T, a p-type diketopyrrolopyrrole-terthiophene polymer with β-branched C_6-C_8 alkyl side-chains, because variations in deposition parameters have been shown to dramatically influence the microstructure of their thin films as deposited by solution shearing.[6,27] Figure 3c shows the rDoC for PDPP3T thin films cast from a 11 mg mL^{-1} tetralin solution at 140°C onto bare Si substrates, where the degree of crystallinity here is normalized to the most crystalline film. This normalization is done because the unit cell for this polymer is not resolved, so an absolute degree of crystallinity cannot be calculated. Contrary to clear trends in simulated strain rate as a function of pillar spacing, it appears that intermediate arrangements yield the most crystalline films. This is not entirely unexpected as there may be some threshold strain rate that is needed to induce an appreciable amount of strain-induced polymer nucleation. Moreover, while moderate strain rates may be sufficient to overcome entropic barriers to effective intermolecular association, stable aggregate formation may still involve a critical nucleus size that is only achievable in regions of high strain rates.

In this way, we expect the strain rates closest to the outlet may be important for overall polymer nucleation. Whereas the spatial distribution of strain rates on the outlet plane appears comparable across all pillar arrays (**Figure S2**), the area-averaged total strain rate across the outlet boundary (**Figure S3**a) appears to be higher for larger interrow b and relatively constant for interpillar a. This contrasts significantly with the trend in Figure 3a, which together suggests that although the volume-averaged Frobenius tensor norm E_{ave} is highest for small a and b, a greater proportion of high-strain regions is close to the outlet when b is higher. This may be the result of the fact that the reduced density of pillars for arrays with greater b allows

for more fluid to move upward (positive z-direction) into the regions between the pillars. In fact, the mass flux through a plane parallel with the tilted coating blade and offset exactly h_p from the blade surface (touching the bottoms of the pillars) indicates that higher a or b increases the mass (and thus volume) flux of fluid *into* the pillar array (Figure S3b). With more fluid flowing within the array and between the pillars, the influence of the pillars is more pronounced.

Statistical analysis of rDoC and simulation results

It is not surprising that the qualitative comparisons previously discussed reveal general trends that indicate the relative degree of crystallinity of deposited films are not strictly monotonic functions. To provide a more rigorous treatment of the data, we opt to apply a formal statistical analysis to the quantitative metrics derived from the simulation. Specifically, we correlate 130 different variables derived from the simulation results (**Table S3**) to the observed rDoC and calculate the correlation coefficient R (also known as the Pearson coefficient). R is a measure of the covariance between two variables, where values very close to $+1$ (or -1) indicate strong positive (or negative) linear dependence. In the case of least-squares regression of a linear model, the commonly seen coefficient of determination R^2 is the square of the Pearson coefficient. However, we emphasize that for our purposes, we are not performing linear regression, and that R serves as a basic metric of correlation between predictor and response. We look at R between the 130 chosen predictor variables and rDoC individually, along with the p-value for the calculate R-values.

There has been much scrutiny in recent years over the use the $p < 0.05$ decision rule to claim that a result is "statistically significant," which can lead to sometimes faulty inference and nonreproducible results.[28,29] As a first step in mitigating the risk of misinterpretation of the statistical analysis, we claim that $0.005 < p < 0.05$ is statistically "suggestive," while $p < 0.005$ is "significant."[30] Furthermore, we also report an approximate upper bound on the Bayes factor, which in this context is defined as the upper bound on the odds that the dependent variable (here, the rDoC) has some linear dependence with the predictor rather than that it has no dependence on the predictor. This transformation provides a more intuitive understanding of the odds that we can reject the null hypothesis (that a functional relationship between the predictor and response does not exist) for the alternative hypothesis (that there is a relationship).[30] We provide more details about this formulation in the Supporting Information section.

The 130 variables analyzed here contain geometric parameters related to the pillar array, average and maximum velocities, average and maximum strain rates $\dot{\gamma}$ and tensor norms $\|\mathbf{E}\|_F$, fluid fluxes across certain simulation boundaries, and each of the matrix elements e_{ij} of $\mathbf{E}$. While the Frobenius norm of $\mathbf{E}$ gives an overall measure of the magnitudes of the rate-of-strain tensor elements, we emphasize that the directional imposition of strain should affect geometry-dependent factors, such as the field-effect mobility. We look not only at average

e_{ij} values for all six unique matrix elements (again, $\mathbf{E}$ is symmetric) as calculated for a given surface or volume, but also their statistical interactions. Interactions in this context are the pairwise multiplicative products of individual variables, which are often used in statistics to determine whether the predictors have coupled effects and thus may not be fully independent variables. We stress that these multiplicative interactions are mathematical constructs that may not necessarily have physical meaning and are used specifically to identify a compounded influence on the response variable. In this study, we choose to look at the interactions for all unique e_{ij} calculated for a given region to determine whether there are any latent dependencies among them in predicting the response. There are thus an additional 15 interaction terms per region of interest.

A summary of results is shown in **Table I**. Out of the analyzed variables, only two exhibit statistically suggestive correlation with the observed relative crystallinity of the resulting thin films: the average strain rate of the x-plane in the x-direction e_x and the average of its interaction with the shear strain rate of the y-plane in the z-direction (or equivalently, the z-plane in the y-direction) $e_x e_{yz}$, both calculated over the outlet plane. We note that e_x is not a shear term, but rather describes the extensional strain rate associated with normal stresses in the x-direction. The R-values themselves, to first order, suggest a correlation of intermediate strength, and their negative magnitudes indicate inverse correlations such that lower (more negative) values of e_x and $e_x e_{yz}$ yield higher rDoC values. While the correlations do not reach our threshold for statistical significance, they are both statistically suggestive. As expected, for the correlations that are statistically significant, their 95% confidence interval bounds (**Table S5**) are farther away from an R-value of zero. If we consider the chance that the outlet-averaged e_x is linearly correlated with rDoC, the odds are at most 4.7 to 1. For reference, the odds of rolling any number (between two and 12) except for seven with two fair, six-sided dice is 5 to 1. For $e_x e_{yz}$, those odds are at most 10.1 to 1; in the card game Blackjack, the odds of losing (going over 21) when you are dealt a 20 and hit is about 11.5 to 1.

Of interest is the fact that the e_x term itself has a correlation with rDoC, whereas e_{yz} does not, suggesting the interaction term $e_x e_{yz}$ is likely dominated by the influence of e_x with some contribution from e_{yz} that leads to better correlation and the lower p-value; this can be seen clearly in plots of the variables in **Figures 5a** and **S4**a. Furthermore, we are not confident in positing a physical explanation for why a shear term in the y- and z-directions is of particular predictive value for the degree of crystallinity. Focusing on e_x, we find that this correlation with an extensional flow term is consistent with studies of polyethylene and traditional homopolymer melts and solutions that have indicated that extensional flow is more effective than shear flow in inducing polymer crystallization.[17,31,32]

Moreover, it has been suspected that the regions of high fluid velocity between the pillars are the regions of polymer elongation and aggregation because of the lateral flow induced,

Table I. The correlation coefficients R and their p-values for all predictors whose linear dependence is at least statistically suggestive ($p < 0.05$).

Dependent Variable	Predictor	R	p-value	BFB
Relative degree of crystallinity	Outlet-averaged e_x	−0.66	0.020	4.7
	Outlet-averaged $e_x e_{yz}$	−0.73	0.007	10.1
Parallel mobility	Outlet-averaged $e_z e_{xy}$	0.62	0.041	2.8
	First-row volume-averaged e_{xy}	−0.82	0.002	27.6
	First-row volume-averaged $e_y e_{xy}$	−0.79	0.004	18.1
	First-row volume-averaged $e_z e_{xy}$	0.80	0.003	20.4
	First-row volume-averaged $e_{xy} e_{yz}$	−0.68	0.022	4.4
Perpendicular mobility	Outlet-volume-averaged $\|\mathbf{E}\|_F$	0.76	0.030	3.5
	First-row volume-averaged velocity V	0.78	0.023	4.3
	Outlet-volume-averaged e_y	0.82	0.013	6.4
	Outlet-volume-averaged $e_y e_{yz}$	0.77	0.027	3.8

The highlighted rows denote candidates that we highlight for predicting crystallinity and field-effect mobilities. Note: BFB, Bayes factor bound.

since regular solution shearing does not induce them.[13] When considering that more negative e_x values are correlated with higher crystallinity, we see from Figure 4 that the flow entering the interpillar region exhibit negative e_x (and also positive e_y) and may be the crucial loci of polymer extension that enhances crystallization. Given that the predictor here is averaged over the outlet plane and not the first-row volume, we conjecture that sustaining high e_x originating in this region and persisting toward the outlet benefits crystallization.

Although film solidification is a downstream process not modeled in these simulations, the correlations revealed here suggest that simulations limited to the fluid flow upstream of the meniscus can guide the optimization of observable properties in the final solid film. This result provides a starting point for further inquiry into determining what combination of variables can predict the crystallinity of the final film and what the underlying mechanism involves.

Charge-transport properties

While overall film crystallinity is of interest when optimizing polymer thin films because of its relationship with enhanced charge-transport properties, the performance metric of interest for organic transistors is the charge-carrier mobility μ. Here, we compare trends in μ of bottom-gate, top-contact transistors fabricated from PDPP3T thin films coated using patterned blades with these array configurations. We plot the

Figure 5. (a) Relative degree of crystallinity as a function of the tensor element e_x averaged over the outlet plane. (b) μ_{para} as a function of the tensor element e_{xy} averaged over the volume of fluid surrounding the row of pillars closest to the outlet.
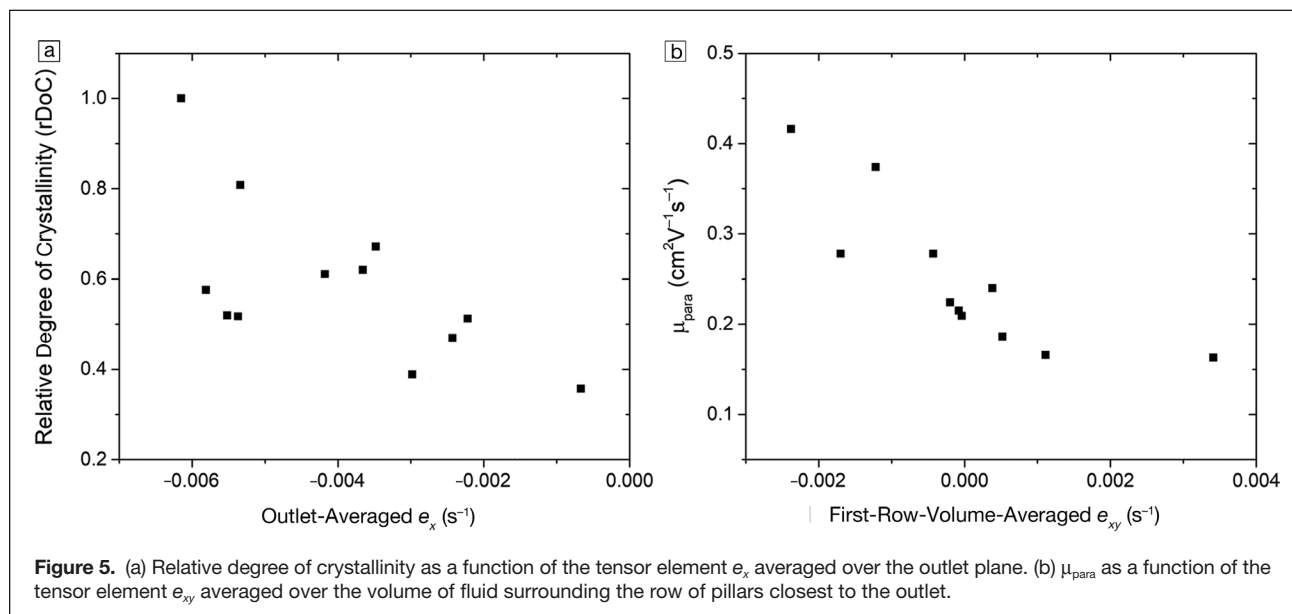
hole mobilities for charge transport in the direction parallel with coating (μ_{para}) and transverse to it (μ_{perp}) in Figures 3d and S3c. We note that μ is a notoriously sensitive parameter that involves factors in addition to deposition-related ones (e.g., polymer chemistry, device architecture, and dielectric quality). Unlike in the case of an unpatterned coating blade, where charge-transport isotropy is attained for all coating speeds,[27] a substantial enhancement in μ_{perp} is seen for some of the films, indicating that the films' microstructure is indeed different from those coated without the patterned blades. Overall, we find that for many pillar configurations, there is an enhancement in charge transport over the reference films coated with a flat, unpatterned blade. Based on these observations, it is likely that μ is affected by the variation in the overall microstructure of the thin films, although it is unclear whether this is the result of an increase in the crystalline fraction.

When we performed a statistical analysis of the results, we found that five predictors indicated correlations with μ_{para} that are at least statistically suggestive. While the interaction term $e_z e_{xy}$ averaged over the outlet plane has a modest correlation with μ_{para}, four predictors are tensor elements and interactions averaged over the fluid volume surrounding the row of pillars closest to the outlet. They consist of e_{xy}, the strongest of the four (Figure 5b), and three interactions with elements in the y- or z-directions. Given the plots of the interaction predictors show strong similarities with e_{xy} by itself (Figure S4b–d), we conclude that e_{xy} is the ostensible underlying factor for the strength of the correlations.

The strongest predictor identified—the first-row volume-averaged e_{xy}—involves shear strain elements related to the y- and x-directions, which correspond to the directions parallel and transverse to the coating direction, respectively. More negative values of e_{xy} correlate with higher μ_{para}. When we observe where the regions of highest shear strain occur, the results are not as clear as for extensional strain. Different arrays exhibit different regions of strong shear strain (**Figure S5**), so it is difficult to implicate *a-priori* a particular part of the simulation box.

As previously mentioned, sufficient strain is known to enhance macromolecular ordering—for semicrystalline polymers, enhanced ordering can be manifested in larger crystallite sizes or better alignment.[33,34] In previous studies of PDPP3T, transmission electron microscope images indicate that the polymer exhibit both small crystallite sizes and charge-transport isotropy despite demonstrating strong optical dichroism, with maximum dichroic ratios of seven.[27] In this case, strong alignment does not result in anisotropic electrical performance. This study suggests that shear strain is nonetheless correlated, at least in part, with better charge transport in the direction parallel to the coating direction, but also that a figure of merit such as charge-carrier mobility results from a variety of factors that cannot be considered in isolation. Given this caveat, these results indicate that, to first-order, a blade design that increases shear strain with respect to the y- and

x-directions may enhance the parallel field-effect mobility of polymer thin films used in transistors.

Of interest is that the simulation region within which averaging occurs for all four of the e_{xy} predictors (the first-row volume) differs from the ones correlated with thin-film crystallinity (the outlet plane). At first glance, we could attribute the stronger correlation of the four predictors to the assertion that high levels of shear strain are directly implicated in higher parallel mobility, so that averaging in the fluid volume where shear strain is the highest provides the clearest correlation signal. However, we cannot neglect the effect of the statistical "binning" we performed in this study to create our set of candidate predictors. It is possible that specific regions near or within the pillar array are more important than others, and that the volume of fluid over which we bin dilutes the signal from regions of differing strain rates actually important for the response variables. In the spirit of introducing in this article statistical analyses of this type to polymer deposition research, we defer more detailed spatial partitioning to future studies.

For charge transport in the direction perpendicular to coating, four other predictors reasonably correlate with the field-effect mobility. Unlike for the degree of crystallinity and μ_{para}, both the volume-averaged fluid velocity V near the first row of pillars and the magnitude of the strain rate tensor **E** near the outlet are positively correlated with μ_{perp} (Figure S4e–f), suggesting that the higher fluid velocities, which can lead to higher overall strain rates, are related to enhanced electrical performance. This is of particular interest because of the inverse relationship between coating speed u and dry film thickness t. In this study, the single u used for each film (0.2 mm s^{-1}) and the choice of solvent, temperature, and solution concentration are all invariant. This combination of variables leads to deposition governed by the evaporative regime[27,35] (also known as convective assembly), under which t approximately varies as u^{-1}. Using higher coating speeds leads to thinner films, so unless other variables are changed, it is not possible to directly compare films of the same thickness with different strain rates vis-à-vis coating speed. In this way, given that film thickness can affect the electrical resistance within measured transistors, it is difficult to isolate the effect of increased fluid velocity on overall electrical performance without changing other deposition parameters. However, we find that our deposited films do not vary systematically with changes in pillar spacings of the arrays studied here and have nominally consistent thicknesses (Table S5). This is slightly unexpected given the differences in volumetric flow rate across the outlet plane (**Table S2**) and suggests that certain phenomena are unaccounted for by the simulation. We suspect these could be related to either flow originating from the meniscus or to concentration gradients within the simulated region or beyond. Nonetheless, in this instance, the use of patterned coating blades allows us to tune the fluid flow during deposition without causing the change of any other deposition-related variables, thus affording us a unique opportunity to observe differences in charge-transport behavior without other confounding factors. The mere

presence of pillars in the flow cavity and their relative spacing locally increase the fluid velocity without substantially altering the film thickness, directly facilitating our investigation of the effect of increased V on μ.

We find here that V does indeed positively correlate with μ_{perp}, and suspect that the correlation with $\|\mathbf{E}\|_F$ (and the fact that $\mathbf{E}$ involves the first spatial derivatives of the components of $\bar{\mathbf{v}}$) also implies that simply increasing the overall fluid velocity is not sufficient to enhance electrical performance—there must be a distribution of local fluid velocities to give rise to higher strain rates. This is exactly what is provided by the coating pillars because they specifically cause fluid to accelerate between them. For the tensor element predictors, we note that the variables that correlate with field-effect mobility in the two directions differ significantly: the primary predictor for μ_{perp} (tensor element e_y, Figure S4g–h) is extensional strain and *not* shear strain, like e_{xy} for μ_{para}. As mentioned earlier, in regular solution shearing without a patterned blade, there is no transverse flow induced (aside from edge effects) in the bulk. We conjecture that such shear strain related to the parallel and perpendicular directions may be important for enhanced macromolecular ordering and improved electrical performance, but primarily when charge transport is in the parallel direction. Indeed, the fact that μ_{perp} is correlated with $\|\mathbf{E}\|_F$ and V but μ_{para} is not suggests that either the ordering mechanisms during deposition differ or that the primary charge-transport mechanism in the two directions (intra- or intermolecular, for example) are sensitive to different fluid flows. If it is the case that the charge-transport mechanism is nominally similar in both directions, it is reasonable to surmise that the charge transport in the two directions may suffer from different types of microstructural defects that are reduced by these different types of flows: shear versus extensional. Alternatively, if the majority charge-transport pathway in a given direction differs in the two directions, these differing flows may induce microstructural enhancements that compensate for the weaker pathway by facilitating better inter- or intramolecular interactions.

Discussion

Previous studies have shown that solid, crescent-shaped pillars added to the coating blade used in solution shearing induce some enhancements in organic semiconductor thin-film morphology. However, we have had a limited understanding of what variables related to the altered fluid flow actually bear association with performance metrics such as in-plane charge-transport mobility. In this study, we have analyzed the qualitative and quantitative differences in the induced velocity fields and have applied a statistical analysis to determine correlations between three figures of merit and 130 proposed predictors.

We found that for our staggered, crescent-shaped pillars, the distance between adjacent pillars in a row (the interpillar distance a) controls the increase in absolute fluid velocity more strong than the distance between pillar rows (the interrow distance b). This primary focus of rapid fluid velocity

occurs within the row of pillars closest to the end of the coating blade (i.e., the outlet in these simulations), and the effect of additional pillar rows appears minimal. Moreover, for a given interpillar distance a, the interrow distance b does not appear to have a substantial effect on the maximum fluid velocities in the regions between pillars. In terms of strain rate, low a and b is crucial for maximizing the volume-averaged total strain rate, while only low a is necessary for achieving maximum total strain rate at some point in the fluid. Regions of positive and negative strain rates are quite localized for the extensional strain terms, but trends in the spatial distribution of shear strain is less clear. The relative degree of crystallinity of PDPP3T thin films deposited using these different pillar arrays does not trend monotonically with increasing a or b, but instead is maximal at intermediate values. While the rDoC approximately trends with the fluid mass flux directly into the pillar array, the results indicate that a deeper statistical analysis of both simulation inputs and the resultant fluid velocity profile is needed to draw quantitative correlations.

Of the 130 variables identified, extensional flow transverse to the coating direction exhibits a statistically suggestive correlation with the resulting thin-film degree of crystallinity when averaged over the outlet plane. It is not surprising that correlations with rDoC are not too strong, because efficient crystallization in polymers depends on a variety of thermodynamic factors not simply attributable to fluid flow. However, for the hole mobility in the parallel direction, a strong correlation is exhibited by the volume-averaged shear strain rate (x-y shear). This contrasts with the predictors for mobility in the perpendicular direction, which indicate that outlet-volume-averaged extensional flow in the coating direction (y extension) is of interest.

We note that in our analysis, we examine linear correlations as a first-order approximation of the real and likely much more complex relationship between the predictors and our response variables. Yet, even with the relative simplicity of a linear model, statistically significant ($p < 0.005$) correlations are revealed. We are particularly encouraged by the ability to correlate important performance metrics—the field-effect mobility and degree of crystallinity—using a simplified simulation that models only fluid flow upstream of the meniscus. While the relative simplicity of modeling only the solution flow near the edge of the coating blade is attractive in its ability to unveiling correlations worthy of future inquiry, we expect that more computationally rigorous modeling of the other components of solid-film formation during solution shearing will enhance the resulting simulation data and yield data sets from which more accurate statistical correlations can be drawn. Specifically, updating the outlet-boundary condition with the effect of interfacial Marangoni flow, and flows directly driven by concentration gradients and indirectly influenced by solvent evaporation flux is important. Others have provided mathematical and experimental treatments of meniscus phenomena,[36–39] and the coupling of these influences on the region studied here would be highly useful. Of particular interest are

how factors such as coating speed, deposition temperature, solution concentration, critical solution concentration for crystallite nucleation, and polymer molecular weight—each of which we believe are major parameters at play—affect the fluid flow within the meniscus and under the coating blade.

Given that a full simulation of the coating process involving the contact line, meniscus, and solution along with processes such as solvent evaporation, interfacial flows, meniscus deformation, concentration-induced flows, and viscosification is computationally infeasible (currently), the results provided by this study of a drastically simplified model of only fluid flow in one specific region, and the actual thin-film microstructure of deposited films is a promising beginning for the use of fluid mechanical simulations to guide coating blade design. By defining useful metrics for comparison and using intuition in terms of what regions of fluid flow are important, we have shown that simplistic models can be useful as both an initial approximation of expected behavior and a guide for deeper, more targeted research.

Materials and methods

Anhydrous 1,2,3,4-tetrahydronaphthalene (tetralin) and anhydrous trichloroethylene (TCE) were purchased from Sigma-Aldrich (USA). n-octadecyltrichlorosilane (OTS) was purchased from Gelest (USA). Degenerately doped n-type, 100> Si wafers with 300-nm-thick thermal oxide layers ($R < 0.005$ Ω cm) were used for transistor fabrication and x-ray diffraction experiments. PDPP3T ($M_w = 22850$ g mol^{-1}, PD = 1.77) was synthesized according to previous reports.[40]

Patterned blade fabrication

Plastic transparency masks for use in photolithography were printed at 20,000 DPI using patterns designed in AutoCAD. The mask consisted of dark (opaque) crescents formed by joining concentric semicircles of radius 10 μm and 20 μm with 4-μm fillets attaching the two arcs. The centers of these semicircles were considered the center of the crescent, which were spaced a apart within a row. The adjacent row was translated a/2 in the lateral direction (y-direction) and b in the coating direction (x-direction). These rows were then repeated so that the pillars would entirely cover a rectangle of about 28 mm × 10 mm, which formed the basis of a coating blade later cut from the wafer.

Four-in. native oxide Si wafers of test grade were primed with hexamethyldisilazane (1,1,1-trimethyl-N-(trimethylsilyl) silanamine, a.k.a. HMDS) at 125°C to promote photoresist adhesion. G/I-line positive photoresist (Shipley 3612) was spincoated to form films with a thickness of 1 μm. The wafers were then baked at 90°C for 60 s. A UV exposure of 1.4 s was performed on a KarlSuss MA-6 aligner with the transparency masks adhered to a blank quartz mask. The wafers were baked at 115°C for 60 s before development in MF-26A (a 2% sol. of tetramethylammonium hydroxide in water). A final bake at 110°C for 60 s was done before inductive charged plasma deep reactive-ion etching was performed. The Bosch process was used for 25 min, during which silicon-etching SF$_6$ plasma alternated with passivating C$_4$F$_8$ plasma to give an etched depth of about 20 μm.

After etching was complete, the remaining photoresist was removed with acetone before oxygen plasma cleaning (150 W, 200 mtorr O$_2$) was used for about 2 min. The wafers were then immersed into a 1% vol. solution of OTS in anhydrous TCE at room temperature for 20 min. They were rinsed with toluene, acetone, and isopropyl alcohol before being baked on a hotplate at 120°C for 20 min. Finally, they were cut with a diamond scribe into individual coating blades for use.

OTS-treated substrate preparation

Transparency masks designed for the substrate consisted of a mostly opaque (black) background with transparent stripes of widths (the direction transverse to the eventual coating direction) ranging between 1.5 mm and 2.5 mm and lengths (parallel with coating) of 4 or 5 mm. The stripes were separated by opaque lines so that the corresponding ratio of transparent to opaque widths were between 2.5 and 5. These arrays of stripes were then arranged so that they could eventually be cut into 2 × 1.5 cm samples, with each sample containing about two rows of stripes with several stripes per row. Because of meniscus instabilities arising from the strongly dewetting OTS-treated substrate surface, the presence of thin lyophilic HMDS regions facilitates easier deposition.

Photolithography was performed as described previously, but with degenerately doped n-type Si wafers with a 300-nm-thick thermal oxide. Instead of using deep reactive ion etching, oxygen plasma cleaning (150 W, 200 mtorr O$_2$) was used for about 5 min to remove the HMDS in the exposed regions.

The substrate wafers were immersed in the OTS solution and baked as described previously, but during the rinse, acetone was not used in order to preserve the photoresist. The result was that the exposed regions then had the OTS-treated surface, and measurements of transistors fabricated using films deposited on these substrates were recorded only for those where the entire channel length and width were on top of the OTS. After baking, the substrates were cut into individual samples, and the photoresist was removed with acetone and gentle brushing with a swab.

Solution shearing

PDPP3T was solution sheared onto each sample from an 11 mg mL^{-1} tetralin solution with a gap height of ≈40 μm, a blade tilt angle of 8°, and a setpoint deposition temperature of 140°C. The substrates and coating blade were cleaned with toluene, acetone, and isopropanol prior to deposition. Each sample was allowed to sit on the heating stage for ≈2 min–3 min to drive off excess solvent after coating.

Field-effect transistor fabrication and measurement

After polymer film deposition onto the OTMS-treated Si/SiO$_2$ substrates, 40-nm-thick Au electrodes were thermally

evaporated through a shadow mask to yield transistor arrays whose channel lengths and widths were 50 and 1000 μm, respectively. These masks produced differently oriented arrays of electrodes such that charge transport could be measured in the direction parallel and perpendicular to the shearing direction. Electrical characterization was performed using a Keithley 4200-SCS semiconductor parameter analyzer. All transistors were in the bottomgate, top-contact geometry (i.e., the silicon substrate acted as a common gate electrode, with the SiO_2 as gate insulator). Each electrode array was electrically isolated by gently scratching the semiconductor film with tweezers. Measurements were carried out in the ambient environment at room temperature, and hole mobilities were extracted in the saturation regime using a drain-source voltage V_{ds} of -100 V.

Crystallinity quantification
For the degree of crystallinity analysis, 2D grazing-incidence, wide-angle x-ray scattering (D-GIWAXS) was performed at the Stanford Synchrotron Radiation Lightsource on beamline 7-2 with an x-ray energy of 15 keV using a Pilatus 300K-W detector oriented horizontally. The films were placed on a sample rotation stage and rotated at 0.5° increments to resolve the (100) reflection as a function of the in-plane angle φ. The horizontal beam width was 100 μm so that the illuminated volume is spatially resolved without reducing photon flux too much. A full scan and a local specular scan[41] of the (100) lamella reflection were measured at α = 0.14° and α ≈ 1.5°, respectively, to construct completes pole figures. The data were integrated in in-plane angle φ because of the strong alignment of these films. The data were corrected by multiplying the intensity at a given polar angle $I(\chi)$ by $\sin \chi$.[42] Data analysis was performed using WxDiff, IgorPro, and MATLAB.

Fluid mechanical simulations
Simulations were performed using COMSOL Multiphysics (version 5.2). The laminar flow option was chosen which, despite the name, still solved the full Navier–Stokes equation. For this geometry, we estimate the Reynolds number when defined using the interpillar spacing a to be on the order of 10^{-2}. We assume Newtonian fluid behavior because the polymer solutions used were relatively dilute. Physics-controlled meshes were computed with a "normal" element size, and a direct solver was chosen using the MUMPS algorithm. The fluid flow was modeled using neat tetralin at a temperature corresponding to the desired deposition conditions modeled; the primary variable this affected in the simulation was the fluid density (0.878 g mL^{-1} at 140°C). Two-dimensional and 3D images were exported directly from COMSOL, and numerical data were extracted for presentation or use in the statistical analysis. Additional details are provided in the Supporting Information section.

Statistical analysis
Calculation of the correlation coefficients R and their corresponding p-values was done using the `corrcoef` function in MATLAB to produce output matrices $\mathbf{R}$ and $\mathbf{P}$. The function relies in part on calculating the covariance matrix of the input, which is an N-by-M matrix, where N is the number of observations, and M is the number of predictors plus one of the three response variables ($M = 130 + 1$). Each of the N rows represents one pillar array and constitutes an independent observation that includes both simulation data (the 130 predictors) and thin-film data (one of the three response variables). N for the rDoC, μ_{para}, and μ_{perp} were 12, 11, and 8, respectively.

Correlations that were at least statistically suggestive were determined by identifying in $\mathbf{R}$ all such values in the row (or equivalently the column, since the output matrices are symmetric) corresponding to the response variable. The p-values for the identified candidates were extracted from the corresponding matrix element in $\mathbf{P}$.

Supplementary material
The supplementary material for this article can be found at https://doi.org/10.1557/mrs.2020.306.

Author contributions
L.S., R.T.W., D.K., M.F.T., and Z.B. designed the experiments. L.S. performed all experiments and simulations. Y.D. and G.C.M.N. contributed to the patterned blade design and their fabrication. Y.D. also facilitated the blade representation in the COMSOL simulation environment. H.Y. assisted with the x-ray measurements. P.H. synthesized the semiconducting polymer. All authors discussed the results and commented on the manuscript.

Competing interests

The authors declare that they have no competing financial interests.

References

1. A. Chortos, J. Liu, Z. Bao, Pursuing prosthetic electronic skin, *Nat Mater*. **15**, 937 (2016).
2. Z. Bao, X. Chen, Flexible and stretchable devices, *Adv. Mater.* **28**, 4177 (2016).
3. J. Kang, J.B.H. Tok, Z. Bao, Self-healing soft electronics, *Nat. Electron.* **2**, 144 (2019).
4. Y. Diao, L. Shaw, Z. Bao, S.C.B. Mannsfeld, Morphology control strategies for solution-processed organic semiconductor thin films, *Energy Environ. Sci.* **7**, 2145 (2014).
5. X. Gu, L. Shaw, K. Gu, M.F. Toney, Z. Bao, The meniscus-guided deposition of semiconducting polymers, *Nat. Commun.* **9**, 534 (2018).
6. L. Shaw, H. Yan, X. Gu, P. Hayoz, R.T. Weitz, D. Kaelblein, M.F. Toney, Z. Bao, Microstructural evolution of the thin films of a donor–acceptor semiconducting polymer deposited by meniscus-guided coating, *Macromolecules* **51**, 4325 (2018).
7. F.L. Lee, A.B. Farimani, K.L. Gu, H. Yan, M.F. Toney, Z. Bao, V.S. Pande, Solution-phase conformation and dynamics of conjugated isoindigo-based donor–acceptor polymer single chains, *J. Phys. Chem. Lett.* **8**, 5479 (2017).
8. D. Mendels, N. Tessler, A comprehensive study of the effects of chain morphology on the transport properties of amorphous polymer films, *Sci. Rep.* **6**, 29092 (2016).
9. K. Maturová, S.S. van Bavel, M.M. Wienk, R.A.J. Janssen, M. Kemerink, Morphological device model for organic bulk heterojunction solar cells, *Nano Lett.* **9**, 3032 (2009).
10. O. Wodo, B. Ganapathysubramanian, Modeling morphology evolution during solvent-based fabrication of organic solar cells, *Comput. Mater. Sci.* **55**, 113 (2012).
11. J. Xu, H.-C. Wu, C. Zhu, A. Ehrlich, L. Shaw, M. Nikolka, S. Wang, F. Molina-Lopez, X. Gu, S. Luo, D. Zhou, Y.-H. Kim, G.-J. N. Wang, K. Gu, V.R. Feig, S. Chen, Y. Kim, T. Katsumata, Y.-Q. Zheng, H. Yan, J.W. Chung, J. Lopez, B. Murmann, Z. Bao, Multiscale ordering in highly stretchable polymer semiconducting films, *Nat. Mater.* **18**, 594 (2019).
12. Y. Diao, B.C.K. Tee, G. Giri, J. Xu, D.H. Kim, H.A. Becerril, R.M. Stoltenberg, T.H. Lee, G. Xue, S.C.B. Mannsfeld, Z. Bao, Solution coating of large-area organic semiconductor thin films with aligned single-crystalline domains, *Nat. Mater.* **12**, 665 (2013).
13. Y. Diao, Y. Zhou, T. Kurosawa, L. Shaw, C. Wang, S. Park, Y. Guo, J.A. Reinspach, K. Gu, X. Gu, B.C.K. Tee, C. Pang, H. Yan, D. Zhao, M.F. Toney, S.C.B. Mannsfeld, Z. Bao, Flow-enhanced solution printing of all-polymer solar cells, *Nat. Commun.* **6**, 7955 (2015).
14. M. Zhong, Y. Li, G. Du, Y. Li, K. Chang, T.-K. Lau, X. Lu, H. Sun, X. Guo, Y.-F. Guo, X. Zhao, W. Deng, Soft porous blade printing of non-fullerene organic solar cells, *ACS Appl. Mater. Interfaces* **12** (23), 25852 (2020).
15. L. Leal, *Advanced Transport Phenomena: Fluid Mechanics and Convective Transport Processes*, Cambridge Series in Chemical Engineering (Cambridge University Press, UK, 2007).
16. R. Aris, *Vectors, Tensors and the Basic Equations of Fluid Mechanics*, Dover Books on Engineering (Dover Publications, New York, 1989).
17. D.E. Smith, H.P. Babcock, S. Chu, Single-polymer dynamics in steady shear flow, *Science* **283**, 1724 (1999).
18. P.R. Schunk, L.E. Scriven, Constitutive equation for modeling mixed extension and shear in polymer solution processing, *J. Rheol.* **34**, 1085 (1990).
19. D. Venkateshvaran, M. Nikolka, A. Sadhanala, V. Lemaur, M. Zelazny, M. Kepa, M. Hurhangee, A.J. Kronemeijer, V. Pecunia, I. Nasrallah, I. Romanov, K. Broch, I. McCulloch, D. Emin, Y. Olivier, J. Cornil, D. Beljonne, H. Sirringhaus, Approaching disorder-free transport in high-mobility conjugated polymers, *Nature* **515**, 384 (2014).
20. R. Noriega, J. Rivnay, K. Vandewal, F.P.V. Koch, N. Stingelin, P. Smith, M.F. Toney, A. Salleo, A general relationship between disorder, aggregation and charge transport in conjugated polymers, *Nat. Mater.* **12**, 1038 (2013).
21. S. Wang, S. Fabiano, S. Himmelberger, S. Puzinas, X. Crispin, A. Salleo, M. Berggren, Experimental evidence that short-range intermolecular aggregation is sufficient for efficient charge transport in conjugated polymers, *Proc. Nat. Acad. Sci. USA* **112**, 10599 (2015).
22. M. Chang, G.T. Lim, B. Park, E. Reichmanis, Control of molecular ordering, alignment, and charge transport in solution-processed conjugated polymer thin films, *Polymers* **9** (6), 212 (2017).
23. A.J. Pennings, Bundle-like nucleation and longitudinal growth of fibrillar polymer crystals from flowing solutions, *J. Polym. Sci.: Polym. Symp.* **59**, 55 (1977).
24. G. Kumaraswamy, J.A. Kornfield, F. Yeh, B.S. Hsiao, Shear-enhanced crystallization in isotactic polypropylene 3, Evidence for a kinetic pathway to nucleation, *Macromolecules* **35**, 1762 (2002).
25. G. Wang, L.-W. Feng, W. Huang, S. Mukherjee, Y. Chen, D. Shen, B. Wang, J. Strzalka, D. Zheng, F.S. Melkonyan, J. Yan, J.F. Stoddart, S. Fabiano, D.M. DeLongchamp, M. Zhu, A. Facchetti, T.J. Marks, Mixed-flow design for microfluidic printing of twocomponent polymer semiconductor systems, *Proc. Nat. Acad. Sci. USA* **117**, 17551 (2020).
26. G. Wang, P.-H. Chu, B. Fu, Z. He, N. Kleinhenz, Z. Yuan, Y. Mao, H. Wang, E. Reichmanis, Conjugated polymer alignment: Synergisms derived from microfluidic shear design and UV irradiation, *ACS Appl. Mater. Interfaces* **8**, 24761 (2016).
27. L. Shaw, P. Hayoz, Y. Diao, J.A. Reinspach, J.W.F. To, M.F. Toney, R.T. Weitz, Z. Bao, Direct uniaxial alignment of a donor-acceptor semiconducting polymer using single-step solution shearing, *ACS Appl. Mater. Interfaces* **8**, 9285 (2016).
28. R.L. Wasserstein, N.A. Lazar, The ASA's statement on p-values: Context, process, and purpose, *Am. Stat.* **70**, 129 (2016).
29. L.G. Halsey, D. Curran-Everett, S.L. Vowler, G.B. Drummond, The fickle P value generates irreproducible results, *Nat. Methods* **12**, 179 (2015).
30. D.J. Benjamin, J.O. Berger, Three recommendations for improving the use of p-values, *Am. Stat.* **73**, 186 (2019).
31. A.J. McHugh, E.H. Forrest, A discussion of nucleation and growth in flow-induced crystallization from solution and an improved model for the growth process, *J. Macromol. Sci. B* **11**, 219 (1975).
32. I.S. Dairanieh, A.J. Mchugh, A.K. Doufas, A phenomenological model for flow-induced crystallization, *J. Reinforced Plast. Compos.* **18**, 464 (1999).
33. M. Chang, Z. Su, E. Egap, Alignment and charge transport of one-dimensional conjugated polymer nanowires in insulating polymer blends, *Macromolecules* **49**, 9449 (2016).
34. M. Chang, D. Choi, E. Egap, Macroscopic alignment of one-dimensional conjugated polymer nanocrystallites for high-mobility organic field-effect transistors, *ACS Appl. Mater. Interfaces* **8**, 13484 (2016).
35. M. Le Berre, Y. Chen, D. Baigl, From convective assembly to Landau-Levich deposition of multilayered phospholipid films of controlled thickness, *Langmuir* **25**, 2554 (2009).
36. F. Doumenc, B. Guerrier, Drying of a solution in a meniscus: A model coupling the liquid and the gas phases, *Langmuir* **26**, 13959 (2010).
37. D.J. Ternet, R.G. Larson, L.G. Leal, Flow-aligning and tumbling in small-molecule liquid crystals: pure components and mixtures, *Rheol. Acta* **38**, 183 (1999).
38. R.Z. Rogowski, A.A. Darhuber, Crystal growth near moving contact lines on homogeneous and chemically patterned surfaces, *Langmuir* **26**, 11485 (2010).
39. G. Jing, H. Bodiguel, F. Doumenc, E. Sultan, B. Guerrier, Drying of colloidal suspensions and polymer solutions near the contact line: Deposit thickness at low capillary number, *Langmuir* **26**, 2288 (2010).
40. J.C. Bijleveld, A.P. Zoombelt, S.G.J. Mathijssen, M.M. Wienk, M. Turbiez, D.M. de Leeuw, R.A.J. Janssen, Poly(diketopyrrolopyrrole-terthiophene) for ambipolar logic and photovoltaics, *J. Am. Chem. Soc.* **131**, 16616 (2009).
41. J.L. Baker, L.H. Jimison, S. Mannsfeld, S. Volkman, S. Yin, V. Subramanian, A. Salleo, A.P. Alivisatos, M.F. Toney, Quantification of thin film crystallographic orientation using X-ray diffraction with an area detector, *Langmuir* **26**, 9146 (2010).
42. L.H. Jimison, S. Himmelberger, D.T. Duong, J. Rivnay, M.F. Toney, A. Salleo, Vertical confinement and interface effects on the microstructure and charge transport of P3HT thin films, *J. Polym. Sci. B Polym. Phys.* **51**, 611 (2013). □